 doi:10.20944/preprints202208.0034.v1

*Article*

# High Sensitivity Sers Substrate of A Few Nanometers Single-Layer Silver Thickness Fabricated by DC Magnetron Sputtering Technology

**Hsing-Yu Wu [1,2,3], Hung-Chun Lin [4], Guan-Yi Hung [5], Chi-Shun Tu [4], Ting-Yu Liu [6], Chung-Hung Hong [7] , Guoyu Yu [8] and Jin-Cherng Hsu [4,9,*]**

1 System Manufacturing Center, National Chung-Shan Institute of Science and Technology, New Taipei City 237209, Taiwan; andy810301@gmail.com
2 Center for Astronomical Physics and Engineering, National Central University, Taipei 320317, Taiwan;
3 Department of Electro-Optical Engineering, National Taipei University of Technology, Taipei 10608, Taiwan
4 Department of Physics, Fu Jen Catholic University, New Taipei City 242062, Taiwan; gguf123tw12345@gmail.com (H-C Lin); chishun.tu@gmail.com (C-S Tu)
5 Department of International Ph.D. Program in Innovative Technology of Biomedical Engineering and Medical Devices, Ming Chi University of Technology, New Taipei City 243303, Taiwan; D091GP002@o365.mcut.edu.tw
6 Department of Materials Engineering, Ming Chi University of Technology, New Taipei City 243303, Taiwan; tyliu@mail.mcut.edu.tw
7 Kidney Research Center, Department of Nephrology, Chang Gung Memorial Hospital, College of Medicine, Chang Gung University, 5 Fu-Shing St., Taoyuan 33333, Taiwan; hongchunghung@gmail.com
8 Department of Engineering and Technology, School of Computing and Engineering, University of Huddersfield, Queensgate Huddersfield, HD1 3DH, England, United Kingdom; G.Yu@hud.ac.uk
9 Graduate Institute of Applied Science and Engineering, Fu Jen Catholic University, New Taipei City 242062, Taiwan
* Correspondence: 054326@mail.fju.edu.tw; Tel.: 886-2-29053765

**Abstract:** Surface-enhanced Raman spectroscopy (SERS) is commonly used for super-selective analysis through nanostructured silver layers in the environment, food quality, biomedicine, and materials science. To fabricate a high-sensitivity but a more accessible device of SERS, dc magnetron sputtering technology was used to realize high sensitivity, low cost, stable deposition rate, and rapid mass production. This study investigated various thicknesses of a silver film ranging from 3.0 to 12.1 nm by field-emission-scanning-electron microscope, X-ray diffraction, and X-ray photoelectron spectroscopy. In the rhodamine 6G (R6G) testing irradiated by a He-Ne laser beam, the analytical enhancement factor (AEF) of $9.35\times10^{8}$, the limit of detection (LOD) of $10^{-8}$ M, and the relative standard deviation (RSD) of 1.61% were better than other SERS substrates fabricated by the same dc sputtering process because the results show that the 6 nm thickness silver layer has the highest sensitivity, stability, and lifetime. The paraquat and acetylcholine analytes were further investigated and high sensitivity was also achievable. The proposed SERS samples were evaluated and stored in a low humidity environment for up to forty weeks, and no spectrum attenuation could be detected. Soon, the proposed technology to fabricate high sensitivity, repeatability, and robust SERS substrate will be an optimized process technology in multiple applications.

**Keywords:** surface-enhanced Raman scattering (SERS); silver nanoparticle (AgNP); rhodamine 6G (R6G); dc magnetron sputtering; SERS substrate; hotspot; analytical enhancement factor (AEF); limit of detection (LOD); relative standard deviation (RSD)

## 1. Introduction

Since the development of Raman spectroscopy in 1928, its measurement spectrum has been applied to many research areas, such as molecular vibrations [1], crystal structures [2-3], and its fingerprint-like specificity [4] to identify the specific chemical structure

 doi:10.20944/preprints202208.0034.v1



[5,6]. In 1974, British scientist Fleischmann discovered the surface-enhanced Raman spectroscopy (SERS) effect to improve the limitation of detecting the dilute molecule concentration Raman-active vibration signal amplified on a rough silver electrode bottom plate by a factor of $10^2$ to $10^4$. The most widely accepted enhanced SERS mechanism is mainly through electromagnetic enhancement (EM) and chemical enhancement (CE) cascade processes. Therefore, the SERS enhancement factor (EF), defined as the product of EM and CE, is described as EF = EM×CE. The EM effect can generally reach $10^2$-$10^3$ times and is more robust than CE [7]. In most cases, the weaker CE spectral signals are amplified through the EM effect. Therefore, the EM effect is a significant factor in influencing SERS sensitivity.

About ten years after the discovery of SERS, the discovered SERS hotspots with silver particle spacing play a dominant role in enhancing the intrinsic Raman signal of the target molecule [8]. The inter-particle distance in silver nano-island arrays of less than 10 nm is crucial for the enhancement [9,10]. Moskovits *et al*. concluded that the light scattered from the molecules was amplified further if striking on nanostructured gold or silver surfaces appropriately. The nanoscale of clefts, gaps, and fissures in nanostructured metals forming the "hotspot" can accumulate incoming light and concentrate the electromagnetic energy to function as an antenna to collect radio waves [11].

Since then, SERS has been a powerful method for analyzing chemical and biological species down to single molecules on surfaces or in solutions [1–5]. The presence of individual analyte molecules can be detected because the relevant characteristic signals are enhanced. SERS is an effective fingerprint analysis technique for real-time field detection of biological and chemical sensing owing to its favorable non-destructive and non-invasive properties [12]. Nowadays, SERS has its characteristics of selectivity, rapidity, simplicity, and specificity and has been widely used in the fields of molecular identification [1], drug monitoring, medical diagnosis, biological detection [5,13], water contaminants [14,15], healthcare [16,17], food safety [18,19], biochemical and medical analysis [20], and bacteria [21].

Another challenging issue of SERS substrates is that the substrates quickly lose their sensitivity and stability when the device is stored in the atmosphere [22]. A wet-chemical synthesis of nanostructures was a technical method to improve atmospheric stability [23-25]. However, the synthesis method is time-consuming and not reproducible for the optimal surface morphology to yield maximum SERS enhancement. To solve this problem, Sha *et al*. deposited the silver nano-island array layer by an electron beam evaporation and a 20 nm thick Au shell by a magnetron sputtering on an Ag@Au core-shell SERS substrate. This method can have good activity in storing a vacuum package [26,27] since the weaker scattering enhancement Au layer on its top acts as a protective layer to anti-oxidation and attenuates the optical background noise. Moreover, the characteristics of the plasmonic fields realize the deposition process based on the nanoparticle shape, and therefore multiple designs of nanostructured platforms are innovated to amplify the Raman response. For example, Minopoli *et al*. found that nano-spheres and nano-bars exhibit better SERS efficiencies at surface coverage broader than 50% due to the higher number of plasmonic hotspots [28].

This study reported a reliable technology to fabricate the SERS substrate of a single silver layer using a dc magnetron sputtering method. Furthermore, compared to the Raman enhancement affected by different layer thicknesses and hotspot regions, the proposed technique deposited the nano-grain layers forming a more uncomplicated structure to manufacture a SERS substrate.

The results show that dilute concentrations of the R6G analyte in $10^{-4}$-$10^{-7}$ M detecting with varying silver monolayer thicknesses of SERS ranging from 3.0-12.1 nm. Further analysis shows that the produced SERS substrates had high sensitivity and low bias when the devices were evaluated by scanning electron microscopy morphology, X-ray diffrac-

Preprints (www.preprints.org) | NOT PEER-REVIEWED | Posted: 2 August 2022 doi:10.20944/preprints202208.0034.v1



tion, X-ray photoelectron spectroscopy (XPS), and Raman spectroscopy. The SERS substrate can detect other molecules, such as paraquat and acetylcholine, and the testing proved that this new SERS device has high sensitivity. In addition, long-lifetime SERS substrates have been investigated that can be stored in a vacuum desiccator or moisture-proof cabinet for up to 40 weeks without losing their sensitivity. All the optimized analyzed data indicate that the SERS technique proposed in this paper can be a candidate stratagem to manufacture SERS substrate for many applications in the near future. This proposed technology will be a candidate method to realize a robust, low-cost, stable deposition rate and high mass production rate.

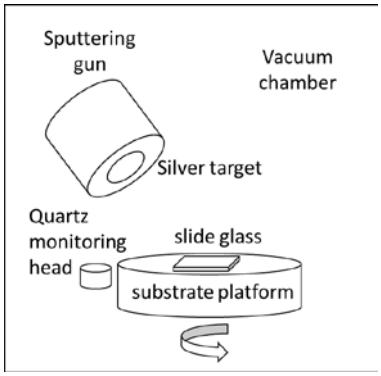


**Figure 1.** Schematic diagram of the sputtering system.

## 2. Materials and Methods

The dimension of glass slide in 76.2×25.4×1 mm was used as the SERS substrate. For the experimental preparation, the substrates were polished with wet cotton, moistened with $CeO_2$ powder, and then ultrasonically cleaned for 20 minutes. After that, the substrates were blown with clean nitrogen gas and then settled in a substrate platform of a vacuum chamber, as shown in Figure 1. The volume of the vacuum chamber is 45 cm in diameter and 50 cm in height. Then, a 5 cm diameter sputtered target loaded with 99.99% metallic silver was mounted approximately 150 mm above the substrate on the sputter gun. In addition, the quartz crystal monitoring head was located near the substrate platform to control a silver thin film.

When conducting the experiments, a diffusion pump drew the base pressure of the chamber to $10^{-5}$ torr. During the deposition process, the working pressure was kept at $3\times10^{-3}$ torr when the working argon gas (99.995%) fed into the chamber at about ten sccm. In this case, the parameters of the dc generator (PFG 1500 DC, made by Huttinger Electronic, Inc. Freiburg, Germany) were 316V voltage and 0.01 A current. The substrate rotation speed was 30 rpm to maintain a uniform thickness of the silver layer. The significant tooling factor is the ratio of actual thickness at a substrate to thickness reading on display. The method to calibrate this factor was to deposit a silver layer about 200 nm thick in a limited time. This process can achieve a relatively stable deposition rate of 0.03 nm/s, monitored by a quartz crystal monitor, and the deposited time for each SERS substrate is discussed in Section 3.1.

**Table 1.** Thicknesses and their relative deposition times for Samples *A-F*.

| Sample | *A* | *B* | *C* | *D* | *E* | *F* |
|---|---|---|---|---|---|---|
| Thickness (nm)* | 3.0 | 4.5 | 6.0 | 7.6 | 9.1 | 12.1 |
| Deposition time (sec) | 79 | 118 | 157 | 196 | 236 | 314 |

* The thickness recorded by a calibrated quartz crystal monitor

To evaluate the sensitivity of the SERS device, their six different silver thicknesses, labeled by Samples *A* to *F*, and their deposition times were prepared and summarized in

 doi:10.20944/preprints202208.0034.v1



Table 1. Before conducting the following examinations, these samples were stored in a moisture-proof cabinet with 25% humidity, a vacuum desiccator, and an air environment. Firstly, a field-emission scanning electron microscope (FESEM, JSM-7600F, Jeol, Tokyo, Japan) was used to analyze the morphologies and cross-sections of the SERS substrates. The as-deposited samples were then characterized by an X-ray diffractometer (Bruker D8 Advance) with CuKalpha radiation ($\lambda$=0.15406 nm). After that, an XPS (ULVAC-PHI, Inc., PHI 5000 VersaProbe III, Kanagawa, Japan) was applied to analyze the chemical bonding state at the surface of the silver layer.

In the aqueous solution testing, R6G, paraquat, and acetylcholine analytes were dropped onto the AgNP layer of the SERS substrates. The Raman spectroscopy (HR Evolution, Horiba, Kyoto, Japan), applied with a 0.1 mW He-Ne laser beam focused by a 100x objective lens, measured the Raman spectrum ranging from 400-2000 $cm^{-1}$.

## 3. Results

### *3.1. Effect of sputtering time on surface morphologies of the silver layers*

The calibrating tooling factor is a fundamental process to produce the required thin film thickness for target sputtered materials. The process was to deposit a 150% tooling factor based on the quartz crystal monitor display. The silver layer with an average 284 nm cross-section shown in Figure 2 was then evaluated by FESEM, and this value was used to adjust the crystal monitor display. Hence, the deposition rate of 0.03 nm/s was derived from the FESEM thicknesses divided by the deposition time. The deposition times from Samples *A* to *F* are reported in Table 1.

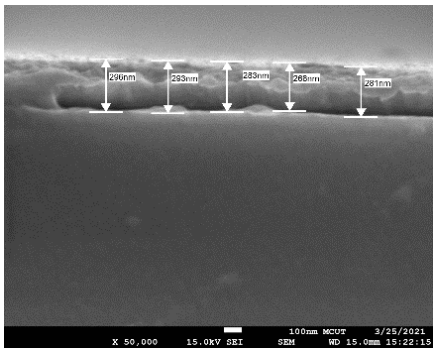


**Figure 2.** FESEM cross-sections of the deposited silver layer for calculating tooling factor.

Figure 3 shows the FESEM morphologies of the silver films deposited at their relative times according to Table 1. The silver nanoparticles of Samples *A* and *B* are transparent. As increasing the deposition time, the nanoparticles grow as Samples *C*, *D*, and *E*. The resulting thickness of Sample *F* forms a liquid-like structure.

Preprints (www.preprints.org) | NOT PEER-REVIEWED | Posted: 2 August 2022 doi:10.20944/preprints202208.0034.v1



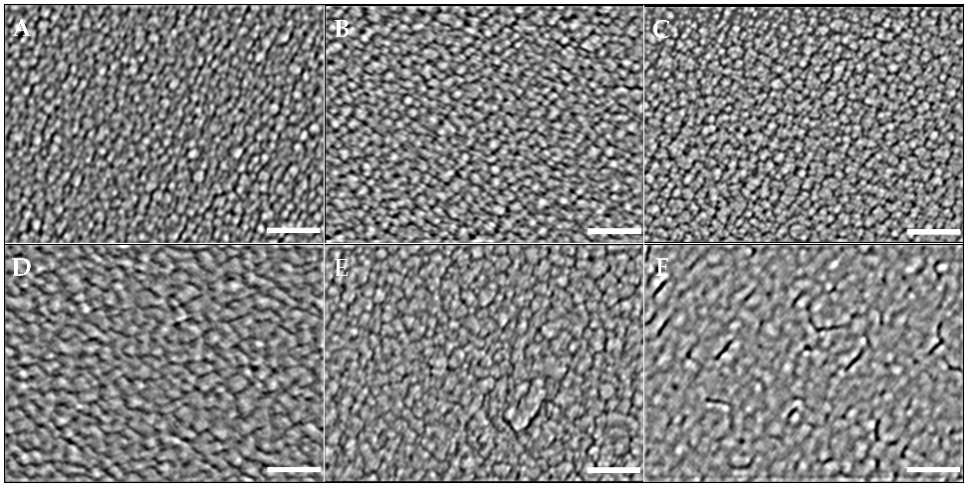


**Figure 3.** Images of FESEM morphologies using the magnification of ×200,000 to analyze Samples *A, B, C, D, E,* and *F*. The size of the white bars in each sub-image is 100 nm. Samples *A-E* show nanoparticle structures, and Sample *F* shows a liquid-like structure.

To further analyze the sizes of nanoparticles and hotspots, ImageJ software provided by the US National Health Institute was applied to analyze the morphological features and quantify the complexity of the digital images [29]. The particle sizes of Samples *A-E* are shown in Figure 4 and summarized in Table 2, where the maximum value ± FWHM/2 represents the sizes, FWHM is the full width half maximum intensity of the Gaussian distribution. Sample *A* has the smallest grain of 18.8±4.5 nm, and Sample *E* has the largest grain of 51.9±10.2 nm. When evaluating the dimension of the hotspot within the five samples, the 50 locations per sample were randomly selected and the resulting average size is approximately 5.3 nm. Sample *F* cannot be evaluated due to the aggregation of the layer.

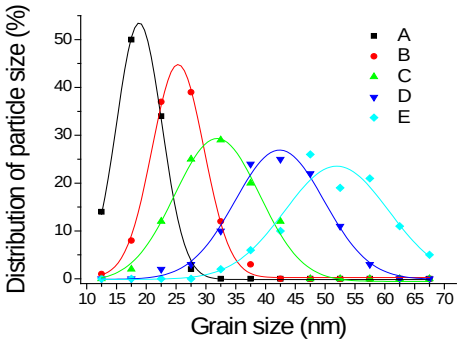


**Figure 4.** The grain sizes of the Samples *A-E* are nearly Gaussian distributions.

**Table 2.** Grain sizes and hotspots for Samples *A-E*.

| Sample | *A* | *B* | *C* | *D* | *E* | *F* |
|---|---|---|---|---|---|---|
| Grain size (nm)* | 18.8±4.5 | 25.3±5.1 | 31.9±8.4 | 42.4±8.3 | 51.9±10.2 | - |
| Hotspot (nm) | 5.30±0.90 | 5.26±0.98 | 5.29±0.94 | 5.32±0.93 | 5.37±0.90 | - |

* Represented by maximum value ± FWHM/2 of Gaussian distribution.

*3.2. XRD of AgNP structures*

Each sample was stored in a vacuum desiccator to prevent silver oxidation when the SERS substrates completed their deposition process. The XRD and XPS were then used to examine the degree of oxidation among the Samples *A-I* with its relative silver thickness of 3.0, 4.5, 6.0, 7.6, 9.1, 12.1, 18.2, 24.2, and 30.3 nm, as shown in Figure 5(a). The measured

Preprints (www.preprints.org) | NOT PEER-REVIEWED | Posted: 2 August 2022 doi:10.20944/preprints202208.0034.v1



XRD peaks at the values of 2$\theta$ are 38.0, 44.2, 64.5, and 78.3°, corresponding to the crystal face structures of Ag(111), Ag(200), Ag(220), and Ag(311), respectively. As for Sample *I*, the apparent polycrystalline of Ag(111) phase and Ag(200) were caused by the thicker silver layer. The face-centered cubic (FCC) crystalline phase measurements were identified as Ag ICDD (International Centre for Diffraction) card number 00-004-0783. Figure 5(b) shows the characteristic diffraction peak of $Ag_2O$(111), which agrees with Ag(I) oxide FCC crystalline phase (JCPDS 041-1104) studied by Rajabi *et al*. [30], associated with different storage of Sample *C* for up to forty weeks. The sample storage in the air environment displays a clear peak because the humidity affects the structure.

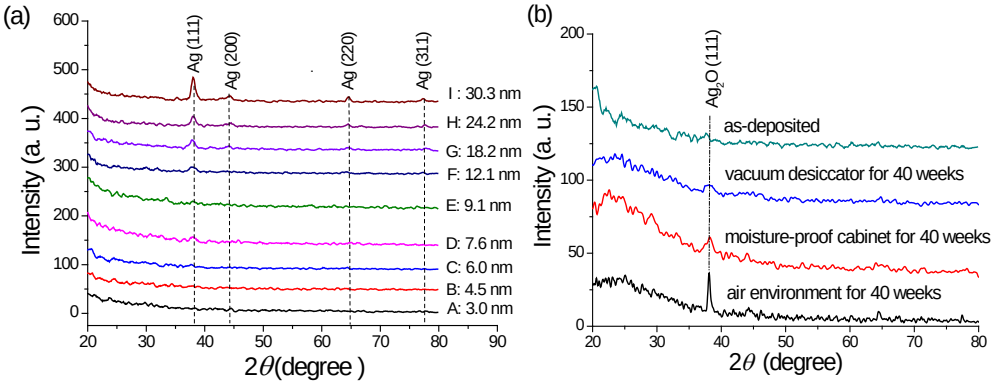


**Figure 5.** (a) XRD patterns of the AgNP layers (Sample *A* to *I*) with various thicknesses (b) XRD measurements of Sample *C* from as-deposited, stored in a moisture-proof cabinet, vacuum desiccator, and air environment for up to forty weeks.

**Table 3.** Crystalline scales of various AgNP layers.

| Sample | Thickness (nm) | FWHM (nm) | Crystalline size (nm) |
|---|---|---|---|
| *A-E* | 3-9.1 | -- | -- |
| *F* | 12.1 | 1.413 | 6.21 |
| *G* | 18.2 | 1.074 | 8.18 |
| *H* | 24.2 | 0.879 | 9.98 |
| *I* | 30.3 | 0.814 | 10.78 |

Each crystalline size of its nanoparticles is determined from the FWHM of the X-ray diffraction pattern according to the dominated direction (111) based on the Scherrer equation [31] described as:

$$D=0.09\lambda/B\cos\theta \quad (1)$$

where *D* is the crystallite size, $\lambda$ is the wavelength of 0.15406 nm using cu-k$\alpha$ radiation, *B* is FWHM, and $\theta$ is the Bragg angle. The thicker the layer, the larger the crystallite scale sizes, as Samples *F-I* are shown in Table 3. However, measuring the crystallite-scale dimensions of Samples *A-E* is difficult because the samples are too thin to measure.

*3.3. X-ray photoelectron spectroscopy of AgNP structures*

Preprints (www.preprints.org) | NOT PEER-REVIEWED | Posted: 2 August 2022 doi:10.20944/preprints202208.0034.v1



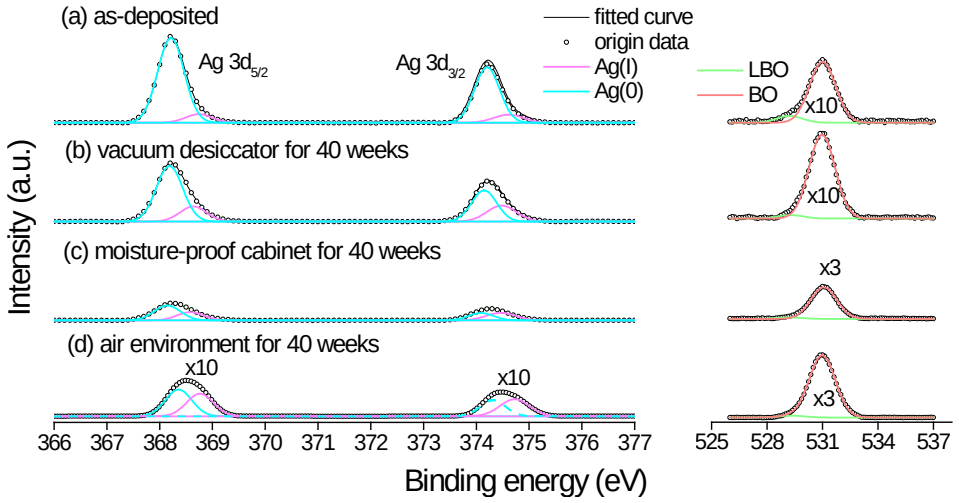


**Figure 6.** High-resolution X-ray photoemission spectroscopy scanning from Ag 3d and O 1s regions.

According to Sample *C* of the optimal SERS substrate discussed in Section 3.4, Sample *C* was selected to be examined by X-ray photoelectron spectroscopy (XPS), in which the binding energy was calibrated by C 1s (284.6 eV). The measurement of the Ag 3d spectrum of AgNPs from high-resolution XPS to evaluate the environmental test is shown in Figure 6. Two peaks centered at ~368.1 and ~374.1 eV are attributed to the binding energies of Ag $3d_{5/2}$ and Ag $3d_{3/2}$, with a splitting energy of 6.0 eV. The FWHMs of the $3d_{5/2}$ and $3d_{3/2}$ peaks of the as-deposit sample are 0.628 and 0.613 eV, respectively. The $3d_{5/2}$ peak was further analyzed to resolute a significant peak of Ag(0) located at 368.2 eV and the fainter peak of Ag(I), which is $Ag_2O$, located at 368.7 eV [32]. C percentage compositions of Ag(0) and Ag(I) elements in Sample C stored in the different environments. O 1s XPS spectra also contained two components, the peak at 531.0 eV with the most significant border area for bridging oxygen (BO) and fainter peaks at 529.2 eV for low-binding-energy oxygen (LBO) [33,34].

**Table 4.** The compositions of Ag(0) and Ag(I) in Sample C stored in the different environments.

| Sample | FWHM of $Ag3d_{5/2}$ | Ag(0) (%) | Ag(I) (%) |
|---|---|---|---|
| as-deposited | 0.628 | 90.7 | 9.3 |
| vacuum desiccator (up to forty weeks) | 0.632 | 78.4 | 21.6 |
| moisture-proof cabinet (up to forty weeks) | 0.801 | 64.1 | 35.9 |
| air environment (up to forty weeks) | 0.939 | 53.9 | 46.1 |

*3.4. Using the SERS samples to detect R6G*

Typical detectable Raman-active modes of R6G probes are summarized in Table 5. Samples *A-F* deposited with their relative silver thickness were used to detect the R6G of $10^{-6}$ M, and the Raman spectra are summarized and illustrated in Figure 7. Many apparent peaks illustrate the signals of the bindings around the R6G molecular.

**Table 5.** Typical Raman Shift of R6G analyte.

| Raman Shift ($cm^{-1}$) | Assignment [35,36] |
|---|---|
| 612 | C-C ring in-plane bending in xanthene rings |
| 771 | C-H out-of-plane bending |
| 1186 | C-H in-plane bending in xanthene ring |
| 1312 | hybrid mode (xanthene rings and $NHC_2H_5$ group) |

Preprints (www.preprints.org) | NOT PEER-REVIEWED | Posted: 2 August 2022 doi:10.20944/preprints202208.0034.v1



| | |
|---|---|
| 1361 | C-C stretching in xanthene ring |
| 1509 | C-C stretching in xanthene ring |
| 1599 | hybrid mode (phenyl ring with $COOC_2H_5$ |
| 1646 | C-C stretching in xanthene ring |

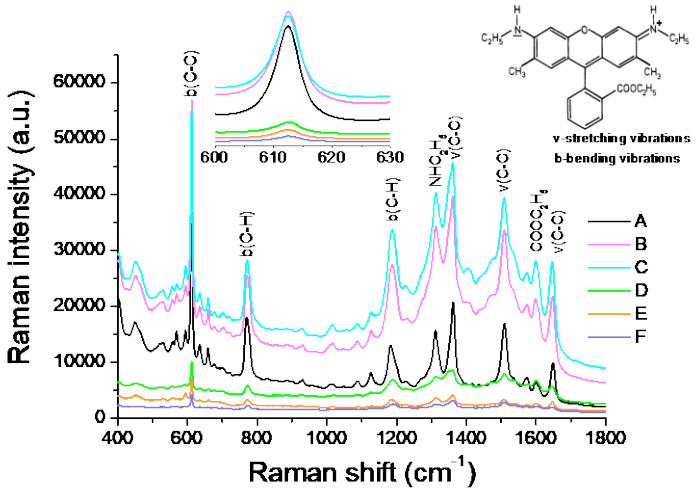


**Figure 7.** SERS spectra resulting from the R6G analyte ($10^{-6}$ M) by the silver layers of the various relative thicknesses.

As shown in the sub-picture in Figure 7, ranging from 600 to 630 $cm^{-1}$, Samples *B* and *C*'s Raman signals and background noises are relatively higher than those of Sample *A*. That is, their Raman enhancement increases with their silver layer thickness. Because the spectra of Figure 7 envelop the enhancement signal and successive background noise, the signal enhancement could be evaluated by the signal-to-background noise ratio (S/B ratio), as shown in Table 6. Sample A seems to receive the largest signal. It is essential to analyze the sensitivity among Samples *A*-*C* further. Figure 8(a) shows the background-subtracted SERS spectra of $10^{-6}$ M R6G analyte on the as-deposited silver substrate with different thicknesses. Sample *C* illustrates the optimal SERS enhancement because all its SERS peaks, except at 612 $cm^{-1}$, are higher than those of the other samples.

**Table 6.** S/B ratios of Samples *A*-*F*.

| **Sample** | ***A*** | ***B*** | ***C*** | ***D*** | ***E*** | ***F*** |
|---|---|---|---|---|---|---|
| **S/B ratio** | 4.63 | 3.15 | 2.64 | 1.94 | 2.18 | - |

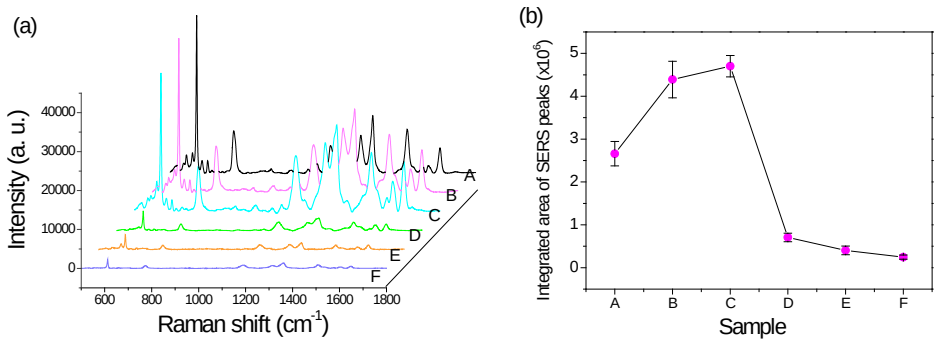


**Figure 8.** (a) Background-subtracted SERS spectra and (b) their integrated intensities of $10^{-6}$ M R6G analyte on different thicknesses of Ag-deposited substrate.

Preprints (www.preprints.org) | NOT PEER-REVIEWED | Posted: 2 August 2022 doi:10.20944/preprints202208.0034.v1



To that end, the integrated area of the background-subtracted SERS spectra was conducted referring to the layer thickness as summarized in Figure 8(b). The integrated intensity increased with the layer's thickness until 6 nm (Sample *C*), then profoundly decreased at 7.6 nm (Sample *D*), and fell to the lowest intensity of 12.1 nm (Sample *F*). Hence, even though the S/B ratio from Sample *A* is larger than Sample *C*, as listed in Table 6, Sample *C* presents the optimal SERS enhancement due to the highest integrated intensity of the SERS spectrum.

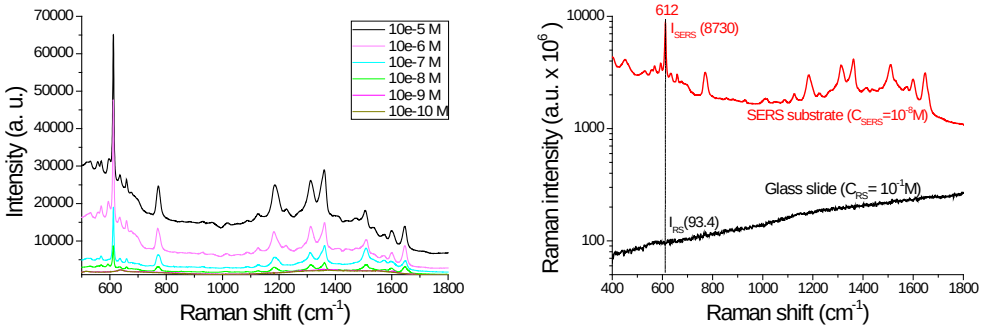


(a) (b)

**Figure 9.** (a) SERS intensities with R6G concentration between $10^{-5}$ to$10^{-10}$ M on Sample *C*. The limit of detection (LOD) observed lower at $10^{-8}$ M. (b) Comparison of the Raman spectra between Sample *C* for measuring $10^{-6}$ M R6G analyte and a pure glass slide for $10^{-1}$ M. .

Then, in Figure 9(a), the various R6G of concentrations from $10^{-5}$ to $10^{-10}$ M were used to determine the sensitivity of Sample *C*, in which the limit of detection (LOD) was $10^{-8}$ M and the analytical enhancement factor (AEF) was $9.35 \times 10^{8}$ evaluated at the 612 $cm^{-1}$ by the following formula,

$$AEF = (I_{SERS}/C_{SERS})/(I_{RS}/C_{RS}) \quad (2)$$

where $I_{SERS}$ (8730) is the measured intensity of the characteristic molecular signal by the SERS substrate in concentration $C_{SERS}$ ($10^{-8}$ M); $I_{RS}$ (93.4) is the intensity by a glass slide in concentration $C_{RS}$ ($10^{-1}$ M), as shown in Figure 9(b).

### *3.5. Reproducibility and storage of SERS substrates*

Reproducible, reliable efficacy, and performance signals are other essential factors to evaluate the SERS substrates. Hence, five random samples of Sample *C* were dropped in a $10^{-6}$ M aqueous R6G solution on five random positions of each substrate to check the repeatability and sensitivity. Figure 10(a) shows all 25 SERS intensities in the 610-615 $cm^{-1}$. The average intensity and the RSD value for Sample C are 46700 and 1.61%, respectively.

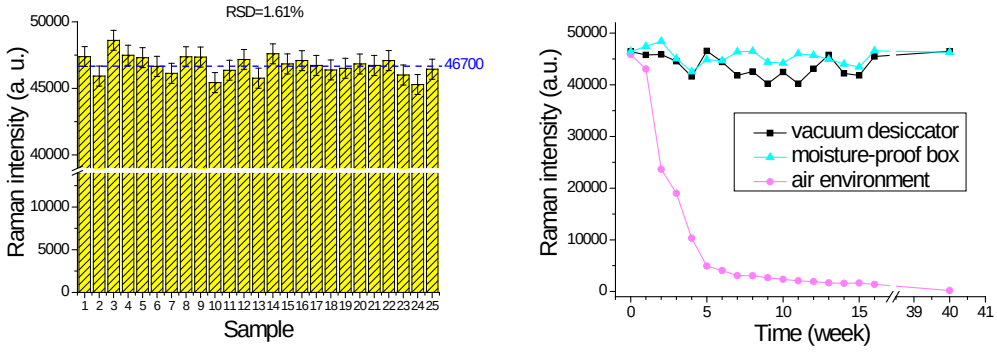


(a) (b)

Preprints (www.preprints.org) | NOT PEER-REVIEWED | Posted: 2 August 2022 doi:10.20944/preprints202208.0034.v1



**Figure 10.** (a) The reproducibility of the SERS substrate evaluated by $10^{-6}$ M concentration of R6G. (b) Lifetime comparisons of SERS Sample C storage up to forty weeks in a vacuum desiccator, a moisture-proof cabinet, and an air environment. .

Another important factor in determining a robust SERS substrate is to evaluate its lifetime. Figure 10(b) shows the Raman intensities of another 54 prepared SERS substrates for Sample *C*, which were separated into three groups to be stored in a vacuum desiccator, a moisture-proof cabinet, and an air environment for up to forty weeks. The samples stored in the vacuum desiccator or moisture-proof cabinet achieved excellent quality. The average SERS intensities of the samples separately stored in the vacuum desiccator and the moisture-proof cabinet were 43600±5% and 45400±3.3% for forty weeks. Only the samples stored in the air environment reduced the intensity to 5000 strength after five weeks.

### *3.6. AEF evaluated by other analytes*

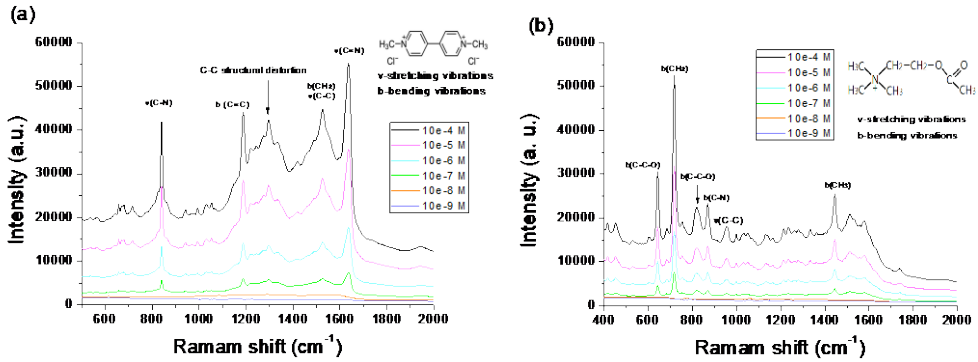


**Figure 11.** Raman spectra from SERS Sample C with various paraquat and acetylcholine analytes concentrations.

Sample *C* was further used to evaluate sensitivity in other analytes. Figure 11(a) and (b) show the excellent performance of the testing in paraquat (e1,1′-dimethyl-4,4′-bipyridinium dichloride, $(C_6H_7N)_2Cl_2$)) and acetylcholine ($CH_3OCOCH_2CH_2N^+$-$(CH_3)_3$), respectively. Paraquat is a highly toxic herbicide that can easily cause poisoning and death to humans and animals [37]. The chemical transmitter acetylcholine is a specific substance that induces nerve stimulation diseases [38]. From the experiments, the proposed SERS substrates can detect paraquat and acetylcholine with the $10^{-7}$ M LOD values of $3.19\times10^7$ and $7.5\times10^7$ AEF values, respectively.

## *4.* Discussion

### *4.1. Effect of sputtering time on surface morphologies of thin silver layers*

As discussed in Table 2, the AgNP sizes of the sputtered layers from 18.8 nm to 51.9 nm were related to the processed deposition time. From Samples A to E, the longer the deposition time, the larger the grain size. Further increasing thickness, as Sample F shows in Figure 3, a liquid-like coalescence began to form on the substrate since the injected silver particles changed the layer's morphology resulting from the lateral growth of the nanoparticles in the longer sputtering time [39]. The processes that include migration of single adatoms on the substrate surface, aggregation of the adatoms, nucleation to form nanoparticles, growth and coalescence of nanoparticles to form a liquid-like structure, and continuous layer formation are associated with the Volmer-Weber growth of high-mobility metal films [40,41].

 doi:10.20944/preprints202208.0034.v1



Table 2 shows the average sizes of the hotspots maintained at about 5.3 nm because of the metallic self-assembly during deposition, as Rastogi *et al*. reported the gold nanoparticle cluster arrays exhibiting less than 10 nm wide inter-cluster hotspots produced on glass [42]. During the deposition, the hotspot physically adsorbed vapor silver atoms, which might move across the surface by hopping from one potential well to another silver adatom assisted by the thermal activation from the surface energy and kinetic energy parallel to the surface. Within the limited residence time at the position of an atom, the atom interacted with the other adatoms and incorporated the surface to form the stable nanograins by releasing condensation heat to less surface energy [43].

Until the AgNP layer's thickness increased to 12.1 nm, the nano-grains agglomerated to the liquid-like structure, as Sample *F* shown in Figure 3, and the number of hotspots further decreased. The continuously deposited silver atoms diffused towards the existing grains on the substrate until the spaces of the hotspots were filled and formed a continuous thin film. The SERS intensity of each sample shown in Figure 7 and Figure 8(a) was related to the AgNP thickness. Hence, it could be concluded that the deposited silver layer of the 6 nm thickness was evaluated as the largest number of hotspots due to the highest SERS sensitivity. This assumption was discussed in Section 4.4.

### *4.2. XRD of AgNP structures*

X-ray diffraction (XRD) was used to discover the formation and crystal structure of silver oxide phases that reacted with oxygen during the deposition process or in the storage environment. Al-Sarraj *et al*. indicated the X-ray diffraction peaks of a silver-oxide film at $2\theta = 32.3^{o}$ and $37.3^{o}$, corresponding to $Ag_2O$ (111) and $Ag_2O$ (200). The AgO was at $2\theta = 34.1^{o}$ and the mixed-phase $Ag/Ag_2O$ formation was $2\theta = 39.6^{o}$ [44]. In our study, no significant intensities of AgO and $Ag_2O$ peaks shown in Figure 5(a) might indicate the high purity silver structure of the stored samples, as studied by Waterhouse *et al*. [45]. The small peaks Ag(220) and Ag(311) also appeared as Shen *et al.* studied in the XPS pattern and Asanithi *et al.* studied in selected-area electron diffraction (SAED) [40,46]. XPS measurements demonstrated the silver oxidation in the following section.

However, Sample *A-E* expresses unapparent XRD diffraction patterns in Figure 5(a). Sagara *et al*. also claimed that the silver crystallite size of 30 to 40 nm could be realized at the 150 nm thickness of the silver thin film deposited by applying the sputtering voltage of 500-600 V at 2 and 4 mtorr [47]. In this study, small peaks of Ag(111), the thicknesses of the layers less than 30.3 nm shown in Table 3, were measured at $2\theta = 38^{\circ}$, and the crystalline sizes were less than 10.78 nm. Moreover, the more significant the crystallite size and the peak, the thicker the deposited thickness. Besides, the diffraction peak of Sample *C*, shown in Figure 5(b), clearly appeared when stored in an air surrounding for forty weeks. The characteristic peaks Ag(111) and $Ag_2O$(111) might overlap at the same diffraction angle. Simultaneously, the translucent light purple of the as-deposited sample changed to translucent light yellow due to an oxidation reaction from humidity. The following section will discuss the oxidation reaction to form the $Ag_2O$ phase.

### *4.3. X-ray photoelectron spectroscopy of AgNP structures*

X-ray photoelectron spectroscopy (XPS) is powerful spectroscopy to measure the surface of a thin film less than 10 nm in thickness. Its qualitative and quantitative results can be used to examine the oxidation state by the photoelectron analysis. It has been reported that only about a 1.2 eV interval exists in spectral features between the Ag $3d_{5/2}$ binding energies of the metallic silver and its oxides. That is, Ag $3d_{5/2}$ is calculated from 367.9 to 368.4 eV for Ag(0) and from 367.6 to 368.5 eV for $Ag_2O$ [48]. The theoretical calculation shows that Ag(I) and Ag(III) are more stable than Ag(II) [49] because most silver oxides, $AgO_x$, $x > 1$, are potent oxidants [50]. The binding-energy intervals of Ag(0), Ag(I), and Ag(III) overlap with each other.

 doi:10.20944/preprints202208.0034.v1



In this study, however, the XPS spectroscopy presented the simple Ag 3d binding energies of Sample *C* stored in the four different environments. All the spectra of the samples only consist of Ag $3d_{5/2}$ and Ag $3d_{3/2}$, as shown in Figure 6. The FWHM for the Ag $3d_{5/2}$ peaks only region 0.628 to 0.939 eV in Table 4. The percentage compositions of the Ag(0) and Ag(I) elements were approximately 90.7% and 9.3%, respectively, indicating that most pure silver element Ag(0) exists in the as-deposited Sample *C*. However, Ag(0) was somewhat decreased to 78.4%, 64.1%, and 53.9% when separately stored in the vacuum desiccator, the moisture-proof cabinet, and the air environment. The enhancement of the O 1s peak intensity indicated the oxidation increase and the oxygen found in AgNP is different from the oxygen in the silver oxides [51], as shown in Figure 6. The prominent BO peak at 531.0 eV represented the oxygen atoms of water molecules from the humidity adsorbed on silver particles; the smaller LBO peak at 529.2 eV was the Ag-O bond of $Ag_2O$. This phenomenon illustrated the apparent humidity intrusion of the AgNP layer stored in the air environment.

### *4.4. SERS detection of R6G*

Figure 8(b) shows the integrated intensities of the background-subtracted SERS spectra. Sample *C* is determined to be the most sensitive among the tested samples resulting from the optimal silver thickness existing the more quantity of hotspots. Sample *C* features the largest contacted surface areas to react with the aqueous solution of R6G analytes to induce the highest SERS signal enhancement. Compared to AgNP structures shown in Figure 3, Sample *F* significantly reduced the SERS enhancement because the continuous thicker silver structure has few hotspots. It is concluded that the thickness and structure of the AgNP layer indeed affect the SERS signal.

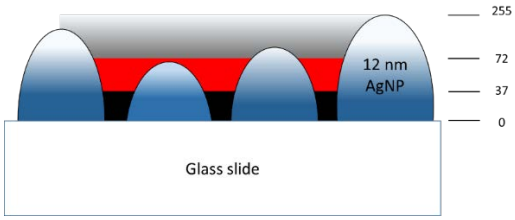


**Figure 14.** Schematic diagram of hotspot region in the thickness direction on Ag-deposited SERS substrate.

Accordingly, the cross-section of the AgNP layer and its relatively active hotspot region is sketched in Figure 14, where the relative greyscales are referenced to various Ag thicknesses from 3.0 nm for Sample *A* to 12.1 nm for Sample *F*. For example, the average brightness of Sample *A* was lower than that of Sample *F* due to the thinner thickness. Then the images of FESEM morphologies in Figure 3 were converted to 0-255 greyscale to represent its three-dimensional structure. Hotspot regions were determined and marked in red between 37 and 72 grayscales, referring to the integrated SERS intensities from the maximum value of $4.7\times10^6$ to the minimum value of $2.5\times10^5$ in Figure 8(b). The hotspot may be generated between layer thicknesses of 1.8±0.9 nm and 3.4±1.7 nm. The grayscale of the other thickness less than 37 was marked in black and that of larger than 72 in grading-grey. This principle was used to transform the FESEM morphology images in Figure 15 to illustrate the hotspot regions according to the layer's thickness.

Preprints (www.preprints.org) | NOT PEER-REVIEWED | Posted: 2 August 2022 doi:10.20944/preprints202208.0034.v1



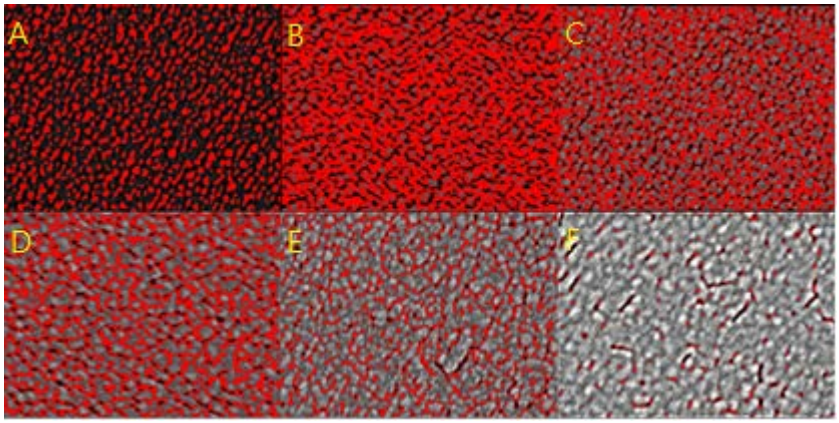


**Figure 15.** Hotspot area on the different Ag-deposited thicknesses on SERS substrates.

Zhang *et al*. also supported this inference that hotspots with their density and along the z-axis in SERS substrates, i.e., increasing the Ag-deposited thickness, can affect the excitation hotspot volume directly [52]. Accordingly, the hotspot volumes for samples A-C were the hotspot area estimated using the software ImageJ multiplied by the thicknesses of silvers. However, there can be two kinds of groove spacing to limit the enhancement of the SERS signal. One is the bottom of the groove spacing without the deposited silver. The bottom area marked in black has fewer hotspots to react with the R6G analytes aqueous solution, such as Sample A shown in Figure 15. The other kind is the top area of groove spacings on the thicker silver layers. The spacings in the top area marked in grading-gray, as shown in Sample E, also have fewer hotspots because their dimensions are larger than the hotspot spacing, where EM between the spacings is too weak to produce the SERS enhancement. In the other case, the thickest Sample F has only a smaller effective thickness to become a small hotspot volume because the R6G analyte has difficulty entering the narrow and deep grooves of the coalesced silver layer due to the cohesion of the solution.

Therefore, the hotspot density varies with the silver's thickness. Figure 16 shows the relative hotspot volume normalized for Sample *C*. The volume of Sample *B* is the largest among the samples. The relative densities of hotspots are the products of the volumes and the relative integrated SERS intensities normalized by the data in Figure 8(b). Sample *C* still owns the largest density of the hotspot. The standard deviation between densities and SERS intensities is only 0.11. That is, the hotspot volumes are expected, as we predicted.

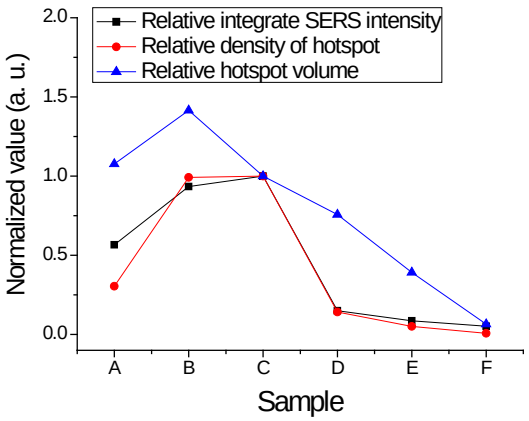


**Figure 16.** Relative densities of hotspots in the AgNP samples.

In addition to the surface enhancement that occurred in the hotspot volume, electromagnetic and chemical enhancements of the SERS are other important conditional factors

Preprints (www.preprints.org) | NOT PEER-REVIEWED | Posted: 2 August 2022 doi:10.20944/preprints202208.0034.v1



[7]. The optimal Sample *C* detection has a LOD value of $10^{-8}$ M, quantified with the SERS intensity at the R6G concentrations between $10^{-5}$ and $10^{-10}$ M, as shown in Figure 9. The LOD value is compared to those of several R6G substrates deposited by the same sputtering technique in several studies over the past three years, as shown in Table 7. Among these published researches, the method of modifying AgNPs on the ferronickel (NiFe) alloy and the cicada wing had a small LODS of $10^{-7}$ M. In our new proposed strategy, sputtering the 6 nm silver layer on a cost-effective commercial glass slide can decrease the LODs to $10^{-8}$ M.

**Table 7.** Comparison of R6G LODs detected on single silver SERS substrate deposited by sputtering methods in several studies in the last three years.

| Material/substrate | LOD of R6G (M) | Year of publication | Reference |
|---|---|---|---|
| Ag/Si | $10^{-4}$ | 2019 | [53] |
| Ag/$SiO_2$ | $10^{-6}$ | 2019 | [54] |
| Ag/Polyester | $10^{-6}$ | 2021 | [55] |
| Ag/PMMA | $10^{-6}$ | 2020 | [56] |
| Ag/ZnO | $10^{-6}$ | 2019 | [57] |
| Ag/NiFe/cicada wing | $10^{-7}$ | 2021 | [58] |
| Ag/ glass slide | $10^{-8}$ | 2022 | This study |

*4.5. Reproducibility and storage of SERS substrate*

Following the optimized SERS substrate of Sample *C*, an AEF of $9.35x10^{8}$ was achieved as assessed by dropping the R6G analyte in a concentration of $10^{-8}$ M, as shown in Figure 9(b). Then, more the SERS samples were prepared by dropping in $10^{-6}$ M to demonstrate their excellent reproducibility, with a high intensity of 46700 and 1.61% RSD, as shown in Figure 10(a). The average intensity of the substrates stored in a moisture-proof cabinet for up to forty weeks achieved 45400±3.3%, which was the same as the as-deposited sample, as illustrated in Figure 10(b). That was, the service life of the substrate was more than forty weeks. Moreover, the SERS substrate remained more sensitive during storage because the moisture-proof cabinet with 25% humidity can dehumidify the substrate surface to prevent moisture intrusion.

*4.6. AEF of different analytes: paraquat and acetylcholine*

To be evaluated the ability of the SERS substrates used to detect other analytes, the AEF values of paraquat and acetylcholine analytes in a concentration of $10^{-6}$ M were $3.19\times10^{7}$ and $7.5\times10^{7}$, respectively, and their LOD values were in $10^{-7}$ M, as shown in Figures 11(a) and (b). Although the AEF values are not outstanding in the SERS substrates fabricated by a chemical method, they are already well performed for physically manufactured substrates. Moreover, the SERS sample manufactured by the dc sputtered technology has promising analyte spectroscopy detection capability and reproducibility. In addition, the processing method in a short time can achieve better stable film thickness control and surface topography than the chemical fabricated SERS substrate. The dc sputtering method to manufacture SERS substrates can be used to realize low-cost and high-volume production. Using this technology to prepare a SERS substrate is expected to achieve high potential applications in real-life, such as agriculture, aquaculture, pastoralism, and mixed contaminants in drinking water, to help the detection of drug hazards and abuse.

## 5. Conclusions

In this study, we successfully prepared silver nanoparticles (AgNPs) with different-sized particles on glass slides for SERS detection by controlling the deposition time of dc sputtering. SEM images show that the thickness and grain size of the films increases with

 doi:10.20944/preprints202208.0034.v1



deposition time. We predict the hotspots can be generated by the dc sputtering between the silver layer thicknesses of 1.8±0.9 nm and 3.4±1.7 nm. Regardless of the deposited thickness of the layers, the hotspot spacing barely changes at about 5.3 nm. The optimal deposited silver thickness on a glass slide is about 6 nm, and the grain size of AgNP is about 31.9 nm. The as-deposited layer investigated by XRD and XPS is a pure silver material, which can enhance the SERS intensity of the dilute R6G analyte with the AEF of $9.35x10^8$ and the LOD of $10^{-8}$ M. The enhancement reproducibility fluctuates in a relative standard deviation of 1.61%, dropping in a $10^{-6}$ M R6G solution. The sensitivity AEF values of this substrate to detect the dilute paraquat and acetylcholine analytes are $3.19\times10^7$ and $7.5\times10^7$, respectively, and the LOD values are $10^{-7}$ M.

The SERS substrate deposited at a 6 nm thickness on glass slides can be prepared by dc sputtering to achieve the characteristics of cost-effectiveness, required stable deposition rate, high mass production rate, and good sensitivity. In addition, the SERS substrates can have a long lifetime of more than forty weeks if stored in a vacuum or moisture-proof environment. These promising results indicate that the fabricated SERS substrate can be a candidate solution to apply to biomolecules, food safety, and environmental pollutants.

**Author Contributions:** Conceptualization, J.-C.H. and H.-Y.W.; methodology, J.-C.H. and H.-Y.W.; software, H.-C.L. and G.-Y.H.; validation, J.-C.H. and H.-C.L.; formal analysis, C.-H.H and H.-C.L.; investigation, H.-C.L. and G.-Y.H.; resources, T.-Y.L. and H.-Y.W.; data curation, J.-C.H. and G.Y.; writing—original draft preparation, J.-C.H.; writing—review and editing, C.-S.T., C.-H.H and H.-Y.W.; visualization, J.-C.H.; supervision, T.-Y.L. and C.-S.T.; project administration, C.-S.T.; funding acquisition, H.-Y.W. and C.-S.T. All authors have read and agreed to the published version of the manuscript.

**Funding:** This research was funded by the Ministry of Science and Technology of Taiwan, grant number MOST 108-2923-M-030-001-MY2 and MOST 110-2112-M-030-003.

**Institutional Review Board Statement:** Not applicable.

**Informed Consent Statement:** Not applicable.

**Data Availability Statement:** The data are included in the article.

**Acknowledgments:** Ming Chi University of Technology supported this FESEM, XPS, and XRD measurement works.

**Conflicts of Interest:** The authors declare no conflict of interest.

## References

1. Wang, W.; Zhao, J.; Short, M.; Zeng, H. Real-time in vivo cancer diagnosis using Raman spectroscopy. *J. Biophotonics.* **2014**, 8, 527.
2. Fernandes, P.A.; Salomé, P.M.P.; Da Cunha, A.F. Study of polycrystalline $Cu_2ZnSnS_4$ films by Raman scattering. *J. Alloy. Compd.* **2011**, 509, 7600.
3. Ansari, M.Z.; Khare, N. Structural and optical properties of CZTS thin films deposited by ultrasonically assisted chemical vapour deposition. *J. Phys. D App. Phys.* **2014**, 47, 185101.
4. McGregor, H.C.; Short, M.A.; McWilliams, A.; Shaipanich, T.; Ionescu, D.N.; Zhao, J.; Wang, W.; Chen, G.; Lam, S.; Zeng, H. Real-time endoscopic Raman spectroscopy for in vivo early lung cancer detection. *J. Biophotonics.* **2016**, 10, 98.
5. He, L.; Natan, M.J.; Keating, C.D. Surface-enhanced Raman scattering: A structure-specific detection method for capillary electrophoresis. *Anal. Chem.* **2000**, 72, 5348.
6. Sil, S.; Umapathy, S. Raman spectroscopy explores molecular structural signatures of hidden materials in depth: Universal multiple angle Raman spectroscopy. *Sci. Rep.* **2014**, 4, 5308.
7. Lane, L.A.; Qian, X.; Nie, S. SERS nanoparticles in medicine: from label-free detection to spectroscopic tagging. *Chem. Rev.* **2015**, 115, 19, 10489–10529.
8. Hao, E.; Schatz, G.C. Electromagnetic fields around silver nanoparticles and dimers. *J. Chem. Phys.* **2004**, 120, 357.
9. Etchegoin, P.G.; Le Ru, E.C. A perspective on single molecule SERS: current status and future challenges. *Phys. Chem. Chem. Phys.* **2008**, 10, 6079.
10. Camden, J.P.; Dieringer, J.A.; Wang, Y.; Masiello, D.J.; Marks, L.D.; Schatz, G.C.; Van Duyne, R.P. Probing the structure of single-molecule surface-enhanced Raman scattering hot spots. *J. Am. Chem. Soc.* **2008**, 130, 12616.
11. Moskovits, M. Spot the hotspot. *Nature*, **2011**, 469, 307-308.

12. Mosier-Boss, P.A. Review of SERS substrates for chemical sensing. *Nanomaterials* **2017**, 7, 146.
13. Liu, T.Y.; Chen, Y.; Wang, H.H.; Huang, Y.L.; Chao, Y.C.; Tsai, K.T.; Cheng, W.C.; Chuang, C.Y.; Tsai, Y.H.; Huang, C.Y.; Wang, D.W.; Lin, C.H.; Wang, J.K.; Wang, Y.L. Differentiation of bacteria cell wall using Raman scattering enhanced by nanoparticle array. *J. Nanosc. Nanotechnolo.* **2012**, 12.
14. BurmáKyong, J.; KyuáLee, E. Ultra-sensitive trace analysis of cyanide water pollutant in a PDMS microfluidic channel using surface-enhanced Raman spectroscopy. *Analyst* **2005**, 130, 1009.
15. Baia, M.; Danciu, V.; Cosoveanu, V.; Baia, L. Porous nano architectures based on TiO2 aerogels and Au particles as potential SERS sensor for monitoring of water quality. *Vib. Spectrosc.* **2008**, 48, 206.
16. Tokel, O.; Inci, F.; Demirci, U. Advances in plasmonic technologies for point of care applications. *Chem. Rev.* **2014**, 114, 5728.
17. Granger, J.H.; Schlotter, N.E.; Crawford, A.C.; Porter, M.D. Prospects for point-of-care pathogen diagnostics using surface-enhanced Raman scattering (SERS). *Chem. Soc. Rev*. **2016**, 45, 3865.
18. Yang, J.; Rorrer, G.L.; Wang, A.X. Bioenabled SERS substrates for food safety and drinking water monitoring. *Int. J. Opt. Photonics.* **2015**, 9448, 944808.
19. Craig, A.P.; Franca, A.S.; Irudayaraj, J. Surface-enhanced Raman spectroscopy applied to food safety. *Annu. Rev. Food. Sci. Technol.* **2013**, 4, 369.
20. Szaniawska, A.; Kudelski, A. Applications of surface-enhanced Raman scattering in biochemical and medical analysis. Front. Chem. 2021, 9, 296.
21. Andrei, C.C.; Moraillon, A.; Larquet, E.; Potara, M.; Astilean, S.; Jakab, E.; Bouckaert, J.; Rosselle, L.; Skandrani, N.; Boukherroub, R.; Ozanam, F.; Szunerits, S.; Gouget-Laemmel, A.C. SERS characterization of aggregated and isolated bacteria deposited on silver-based substrates. *Anal. Bioanal. Chem.* **2021**, 413, 1417-1428.
22. Haynes, C.L.; McFarland, A.D.; Van Duyne, R.P. Surface-enhanced Raman spectroscopy. *Anal. Chem.* **2005**, 77.
23. Liu, Z.; Yang, Z.; Peng, B.; Cao, C.; Zhang, C.; You, H.; Xiong, Q.; Li, Z.; Fang, J. Highly sensitive, uniform, and reproducible surface-enhanced Raman spectroscopy from hollow Au-Ag alloy nano urchins. *Adv. Mater.* **2014**, 26, 2431.
24. Chan, T.Y.; Liu, T.Y.; Wang, K.S.; Tsai, K.T.; Chen, Z.X.; Chang, Y.C.; Wang, C.H.; Wang, J.K.; Wang, Y.L. SERS detection of biomolecules by highly sensitive and reproducible Raman-enhancing nanoparticle array. *Nanoscale Res. Lett.* **2017**, 12, 344.
25. Larki, P.; Sabri, Y.M.; Kabir, K.M.; Nafady, A.; Kandjani, A.E.; Bhargava, S.K. Silver/gold core/shell nanowire monolayer on a QCM microsensor for enhanced mercury detection. *RSC Adv*. **2015**, 5, 92303.
26. Sha, P.; Su, Q.; Dong, P.; Wang, T.; Zhu, C.; Gao, W.; Wu, X. Fabrication of Ag@Au (core@shell) nanorods as a SERS substrate by the oblique angle deposition process and sputtering technology. *RSC Adv*. **2021**, 11, 27107-27114.
27. Syu, W.L.; Lin, Y.H.; Paliwal, A.; Wang, K.S.; Liu, T.Y. Highly sensitive and reproducible SERS substrates of bilayer Au and Ag nano-island arrays by thermal evaporation deposition. *Surf. Coat. Technol*. **2018**, 350, 823-830.
28. Minopoli, A.; Acunzo, A.; Della Ventura, B.; Velotta, R. Nanostructured surfaces as plasmonic biosensors: A review. *Adv. Mater. Interf.* **2021**, 9, 2101133.
29. http://rsb.info.nih.gov/ij/plugins/fraclac/FLHelp/Introduction.htm
30. Rajabi, A.; Ghazali, M.J.; Mahmoudi, E.; Baghdadi, A.H.; Mohammad, A.W.; Mustafah, N.M.; Ohnmar, H.; Naicker, A. S. Synthesis, characterization, and antibacterial activity of Ag2O-loaded polyethylene terephthalate fabric via ultrasonic method. Nanomaterials 2019, 9, 450.
31. Scherrer, P. Bestimmung der inneren Struktur und der Größe von Kolloidteilchen mittels Röntgenstrahlen. In: Kolloidchemie Ein Lehrbuch. Springer, Berlin, Heidelberg, Germany 1912. p. 387-409.
32. Gard, F.S.; Daizo, M.B.; Santos, D.M.; Halac, E.B.; Freire, E.; Reinoso, M.; Bozzano, P.B.; Dominguez, S.A.; Montero, R.J. Application of surface science techniques to study a gilded Egyptian funerary mask: A multi-analytical approach. *Surf. Interface Anal.* **2019**, 51, 1001-1017.
33. Hsu, J.C., Wang, P.W., Lee, C.C. X-ray photoelectron spectroscopy study of thin $TiO_2$ films cosputtered with Al. *Appl. Opt*. **2006**, 45, 4303-4309.
34. Hsu, J.C.; Lee, C.C.; Chen, H.L.; Kuo, C.C.; Wang, P.W. Investigation of thin TiO2 films cosputtered with Si species. *Appl. Surf. Science*. **2009**, 255, 4852-4858.
35. Watanabe, H.; Hayazawa, N.; Inouye, Y.; Kawata, S. DFT vibrational calculations of rhodamine 6G adsorbed on silver: Analysis of tip-enhanced Raman spectroscopy. *J. Phys. Chem. B* **2005**, 109, 5012-5020.
36. Hildebrandt, P.; Stockburger, M. Surface-enhanced resonance Raman spectroscopy of rhodamine 6G adsorbed on colloidal silver. *J. Phys. Chem.* **1984,** 88, 5935-5944.
37. Suntres, Z.E. Role of antioxidants in paraquat toxicity. *Toxicology* **2002,** 180, 65-77.
38. Eccles, J.C. The Synapse: From electrical to chemical transmission. *Annu. Rev. Neurosci.* **1982**, 5, 325-339.
39. Osipov, A.V. Kinetic model of vapor-deposited thin film condensation: stage of liquid-like coalescence. *Thin Solid Films* **1995**, 261, 173-182.
40. Asanithi, P.; Chaiyakun, S.; Limsuwan, P. Growth of silver nanoparticles by DC magnetron sputtering. *J. Nanomater.* **2012**, 2012.
41. Abadias, G.; Simonot, L.; Colin, J.J.; Michel, A.; Camelio, S.; Babonneau, D. Volmer-Weber growth stages of polycrystalline metal films probed by in situ and real-time optical diagnostics. *Appl. Phys. Lett.* **2015**, 107, 183105.

42. Rastogi, R.; Dogbe Foli, E.A.; Vincent, R.; Adam, P.M.; Krishnamoorthy, S. Engineering electromagnetic hotspots in nanoparticle cluster arrays on reflective substrates for highly sensitive detection of (bio)molecular analytes. *ACS Appl. Mater. Interfaces* **2021**, 13, 32653-32661.
43. Chopra, K.; Klerrer, J. Thin film phenomena. *J. Electrochem. Soc.* **1979**, 117, 138.
44. Al-Sarraj, A.; Saoud, K.M.; Elmel, A.; Mansour, S.; Haik, Y. Optoelectronic properties of highly porous silver oxide thin film. *SN Appl. Sci.* **2021**, 3, 1-13.
45. Waterhouse, G.I.; Bowmaker, G.A.; Metson, J.B. The thermal decomposition of silver (I, III) oxide: A combined XRD, FT-IR and Raman spectroscopic study. *Phys. Chem. Chem. Phys.* **2001**, 3, 3838-3845.
46. Shen, Z.; Luo, Y.; Wang, Q.; Wang, X.; Sun, R. High-value utilization of lignin to synthesize Ag nano-particles with detection capacity for Hg2+. *ACS Appl. Mater. Interfaces* **2014,** 6, 16147-16155.
47. Sagara, R.; Kawamura, M.; Kiba, T.; Abe, Y.; Kim, K.H. Characteristics of Ag thin films sputter deposited using Ar or Kr gas under different pressure. *Surf. Coat. Technol.* **2020**, 388, 125616.
48. Wagner, C.D.; Naumkin, A.V.; Kraut-Vass, A.; Allison, J.W.; Powell, C.J.; Rumble Jr, J.R. NIST X-ray photoelectron spectroscopy database, NIST Standard Reference Database 20, Version 3.4 (Web Version). *US Department of Commerce* **2003**, 1.
49. Tudela, D. Silver(II) oxide or silver(I,III) oxide? *J. Chem. Educ.* **2008**,85, 863.
50. Fischer, P.; Jansen, M.; Zahurak, S.M. Electrochemical syntheses of binary silver oxides. *Inorganic Syntheses: Nonmolecular Solids* **1995**, 30, 50-55.
51. Schön, G.; Tummavuori, J.; Lindström, B.; Enzell, C.R.; Enzell, C.R.; Swahn, C.G. ESCA studies of Ag, Ag2O and AgO. *Acta Chem. Scand*, ***1973***, 27, 2623.
52. Zhang, Q.; Lee, Y.H.; Phang, I.Y.; Lee, C.K.; Ling, X.Y. Hierarchical 3D SERS substrates fabricated by integrating photolithographic microstructures and self-assembly of silver nanoparticles. *Small* **2014**, 10, 2703-2711.
53. Yun, S.; Lee, D.; Kim, B.; Cho, C. Highly manufacturable nanoporous Ag films using new sputtering system for surface enhanced Raman scattering substrate. *J. Nanosci. Nanotechnol.* **2019**, 19, 6429-6436.
54. Mu, J.J.; He, C.Y.; Sun, W.J.; Guan, Y. Selective synthesis of three-dimensional ZnO@Ag/SiO2@Ag nanorods arrays as surface-enhanced Raman scattering substrates with tunable interior dielectric layer. *Chin. Phys. B* **2019**, 28, 124204.
55. Bian, X.; Xu, J.; Yang, J.; Chiu, K.; Jiang, S. Flexible Ag SERS substrate for non-destructive and rapid detection of toxic materials on irregular surface. *Surf. Interfaces* **2021**, 23, 100995.
56. Zhang, W.; Tian, Q.; Chen, Z.; Zhao, C.; Chai, H.; Wu, Q.; Li, W.; Chen, X.; Deng, Y.; Song, Y. Arrayed nanopore silver thin films for surface enhanced Raman scattering. *RSC Adv.* **2020**, 10, 23908-23915.
57. Tieu, D.T.; Quynh Trang, T.N.; Tuan Hung, L.V.; Hanh Thu, V.T. Assembly engineering of Ag@ZnO hierarchical nanorod arrays as a pathway for highly reproducible surface-enhanced Raman spectroscopy applications. *J. Alloys Compd.* **2019**, 808, 151735.
58. Zhang, A.; Guo, L.; Li, N.; Zhu, Y.; Jiao, T.; Wang, M. Research on the Raman properties of NiFe/cicada wing composite SERS platform modified by silver nanoparticles. *Curr. Appl. Phys.* **2021**, 25, 24-32.